

Proximity-induced superconducting gap in the quantum spin Hall edge state of monolayer WTe_2

Felix Lüpke,^{1*} Dacen Waters,^{1*} Sergio C. de la Barrera,¹ Michael Widom,¹
David G. Mandrus,^{2,3,4} Jiaqiang Yan,² Randall M. Feenstra,¹ and Benjamin M. Hunt^{1†}

¹ *Department of Physics, Carnegie Mellon University, Pittsburgh, PA 15213, USA*

² *Materials Science and Technology Division, Oak Ridge National Laboratory, Oak Ridge, TN 37831, USA*

³ *Department of Materials Science and Engineering, University of Tennessee, Knoxville, TN 37996, USA*

⁴ *Department of Physics and Astronomy, University of Tennessee, Knoxville, TN 37996, USA*

* These authors contributed equally

†E-mail: bmhunt@andrew.cmu.edu

The quantum spin Hall (QSH) state was recently demonstrated in monolayers of the transition metal dichalcogenide $1\text{T}'\text{-WTe}_2$ and is characterized by a band gap in the two-dimensional (2D) interior and helical one-dimensional (1D) edge states [1–3]. Inducing superconductivity in the helical edge states would result in a 1D topological superconductor, a highly sought-after state of matter [4]. In the present study, we use a novel dry-transfer flip technique to place atomically-thin layers of WTe_2 on a van der Waals superconductor, NbSe_2 . Using scanning tunneling microscopy and spectroscopy (STM/STS), we demonstrate atomically clean surfaces and interfaces and the presence of a proximity-induced superconducting gap in the WTe_2 for thicknesses from a monolayer up to 7 crystalline layers. At the edge of the WTe_2 monolayer, we show that the superconducting gap coexists with the characteristic spectroscopic signature of the QSH edge state. Taken together, these observations provide conclusive evidence for proximity-induced superconductivity in the QSH edge state in WTe_2 , a crucial step towards realizing 1D topological superconductivity and Majorana bound states in this van der Waals material platform.

Contemporary interest in topological superconductors has been driven by potential applications of their gapless boundary excitations, which are thought to be emergent Majorana quasiparticles with non-abelian statistics [5–8]. One path toward topological superconductivity is to realize an intrinsic spinless p -wave superconductor [9]. A powerful alternative is by using a conventional s -wave superconductor to induce Cooper pairing in topologically non-trivial states via the superconducting proximity effect, resulting in an effective p -wave pairing [10]. This approach has recently been employed to engineer 2D topological superconductivity in epitaxial three-dimensional topological insulator films grown on a superconducting substrate [11, 12], and 1D topological superconductivity by proximitizing a 2D QSH system in buried epitaxial semiconductor quantum wells [13, 14]. While such demonstrations mark important milestones, there are clear advantages for exploring topological superconductivity in the van der Waals material platform. Using layered 2D materials allows the 2D QSH edge to be proximitized in vertical heterostructures, circumventing the length restrictions of lateral proximity-effect geometries. Furthermore, the surfaces and

edges are readily available for surface probes, allowing detection and fundamental study of signatures of the topological superconducting state. Following recent theoretical predictions [15], an intrinsic QSH state was demonstrated in a monolayer (ML) of $1\text{T}'\text{-WTe}_2$ [1–3, 16–18]. WTe_2 is attractive for studying the QSH edge modes because it can be readily incorporated in van der Waals heterostructures and has shown quantized edge conductance up to 100 K [3]. Furthermore, ML WTe_2 was recently also shown to host intrinsic superconducting behavior below ~ 1 K when electrostatically gated into the conduction band [19, 20].

In the present work, we study mechanically-exfoliated single- and few-layers of WTe_2 which have been transferred onto the van der Waals s -wave superconductor NbSe_2 . We show that this approach induces a superconducting gap in the WTe_2 without the need for electrostatic doping and yields a critical temperature much higher than that of the intrinsic WTe_2 superconductivity, an experimental advantage which greatly facilitates studies of the interplay of superconductivity and the QSH edge modes. We employ scanning tunneling microscopy and spectroscopy (STM/STS) to investigate the proximity-induced superconducting gap as a function of temperature, magnetic field, and WTe_2 thickness. By spatially resolving the spectroscopic features of the WTe_2 , we find that the superconducting gap coexists with the QSH signature at the ML WTe_2 edge, demonstrating critical steps toward identifying 1D topological superconductivity in a van der Waals material system.

We have developed a novel fabrication technique which enables the assembly and deterministic placement of van der Waals heterostructures in a glove box (Fig. 1a). Though similar methods have been used to fabricate complex encapsulated mesoscale devices [21], critically, our technique produces atomically-clean surfaces of air-sensitive materials suitable for high-resolution scanning probe measurements. In detail, WTe_2 and NbSe_2 are exfoliated from bulk materials and assembled using a PPC/PDMS stamp inside a nitrogen-filled glove box. Subsequently, the PPC film is peeled off, flipped upside down and put onto a second PDMS stamp which has a hole cut into it. This stamp is used to deterministically place the heterostructure onto a pre-patterned gold lead on a SiO_2 chip which is mounted and contacted to an STM sample plate. The PPC is then removed by annealing under vacuum condi-

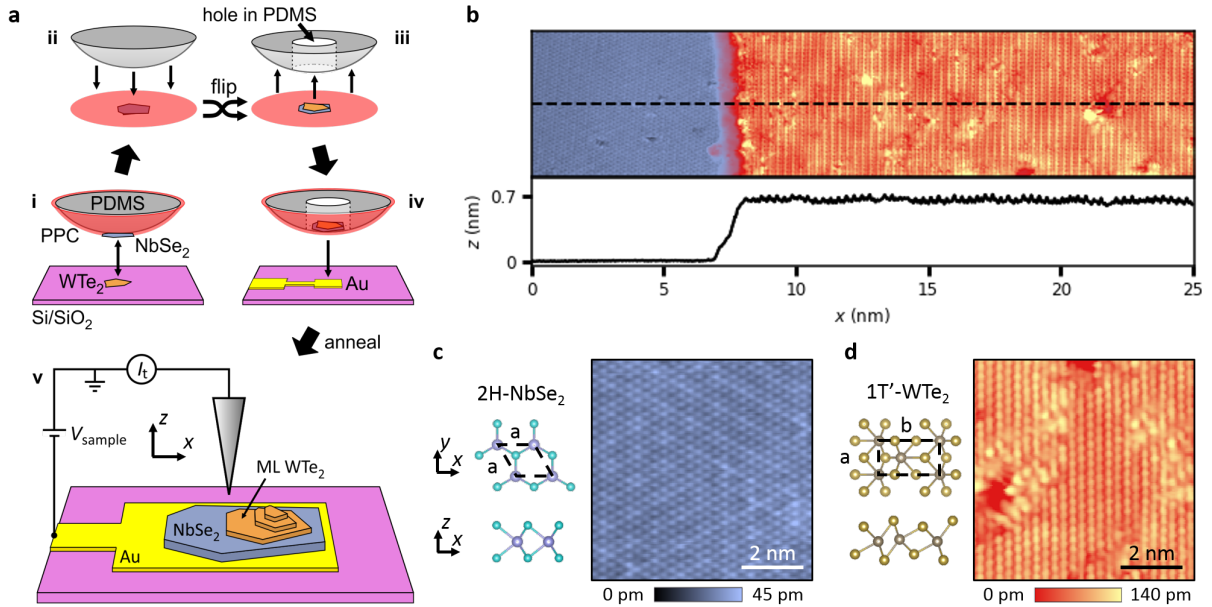


FIG. 1. **Fabrication and morphology of $\text{WTe}_2/\text{NbSe}_2$ heterostructure.** (a) Schematic of the sample fabrication and measurement setup. (b) STM topography and height profile across the edge of the monolayer WTe_2 flake ($V_{\text{sample}} = 300$ mV and $I_t = 10$ pA). (c) Atomic structures and atomically-resolved STM image of the NbSe_2 flake showing the 3×3 CDW ($V_{\text{sample}} = 300$ mV and $I_t = 35$ pA). (d) Atomic structures and atomically-resolved STM image of ML WTe_2 ($V_{\text{sample}} = 1$ V and $I_t = 55$ pA). The topographies shown in (b), (c), and (d) are representative of the heterostructure over most of the area of the exfoliated flakes.

tions and the sample is transferred to the STM, all without intermediate air-exposure and without bringing the heterostructure surface into contact with any polymers or solvents, ensuring the surface cleanliness (for further details see Supplementary Materials). Figure 1b shows an STM image of the resulting heterostructure where the WTe_2 ML edge and the underlying NbSe_2 are visible, showing atomically-clean surfaces on each material. The profile across the step edge shows a step height of ~ 7 Å which corresponds to one WTe_2 layer [17], indicating an atomically-clean interface between the WTe_2 and NbSe_2 . In Fig. 1b a weak moiré pattern in the form of diagonal stripes can be seen on the ML WTe_2 resulting from the superposition of the two different atomic lattices. The moiré pattern, analyzed in more detail in the Supplementary Materials, corresponds to a twist angle of $\approx 3^\circ$ between the NbSe_2 hexagonal unit cell with lattice parameters $a = 3.44$ Å and WTe_2 rectangular unit cell with lattice parameters $a = 3.48$ Å and $b = 6.28$ Å (Fig. 1c, d). Atomically-resolved STM images of the NbSe_2 surface (Fig. 1c) show the well-known 3×3 charge density wave [11], indicating the pristine quality of the NbSe_2 flake. Atomically-resolved STM images of the WTe_2 (Fig. 1d) are characterized by vertical atomic rows parallel to the a -axis of the WTe_2 unit cell.

Turning now to spectroscopic analysis of these surfaces, Fig. 2a shows a series of dI/dV spectra taken along a line perpendicular to the WTe_2 ML step edge (upper panel) and the corresponding height profile (lower panel). The dI/dV spectra clearly show the presence of an increased local density of states (LDOS) near the WTe_2 step edge. This feature was

recently reported in STM/STS studies of ML films of WTe_2 grown on epitaxial graphene substrates [1, 16]. Based on combined evidence from angle-resolved photoemission spectroscopy (ARPES) and STS in Ref. 1, it was concluded that ML WTe_2 has a band gap of (56 ± 14) meV, and that the increased LDOS at the ML WTe_2 edge signifies the metallic QSH edge state. In our monolayer samples, produced via isolation from bulk crystals rather than molecular beam epitaxy, and on superconducting substrates rather than graphene, we observe the same spectroscopic features, which we attribute to the same QSH edge state. Figure 2b shows the averaged dI/dV spectrum on the WTe_2 ML (red) and the ML edge (orange) at the corresponding positions indicated in Fig. 2a. The spectroscopic signature of the QSH edge state is evident primarily in the valence band but, importantly, the edge state also crosses the band gap. Following the interpretation of Ref. 1, the increases in the dI/dV signal at $E - E_F \approx -50$ meV and $E - E_F \approx 15$ meV correspond to the onset of the WTe_2 valence and conduction band, respectively, locating E_F in the ML WTe_2 band gap. A non-zero dI/dV signal in the band gap away from the step edge was proposed to be due to defect states and substrate effects [1]. In addition, tip-induced band bending may play a role in introducing spectral weight in the WTe_2 band gap (see Supplementary Materials). By comparing the positions of the observed spectral features to epitaxially-grown WTe_2 on graphene [1, 16] and exfoliated WTe_2 [22], we conclude that there is no significant charge transfer from the NbSe_2 to the WTe_2 . This observation is further supported by our density functional theory (DFT) calcu-

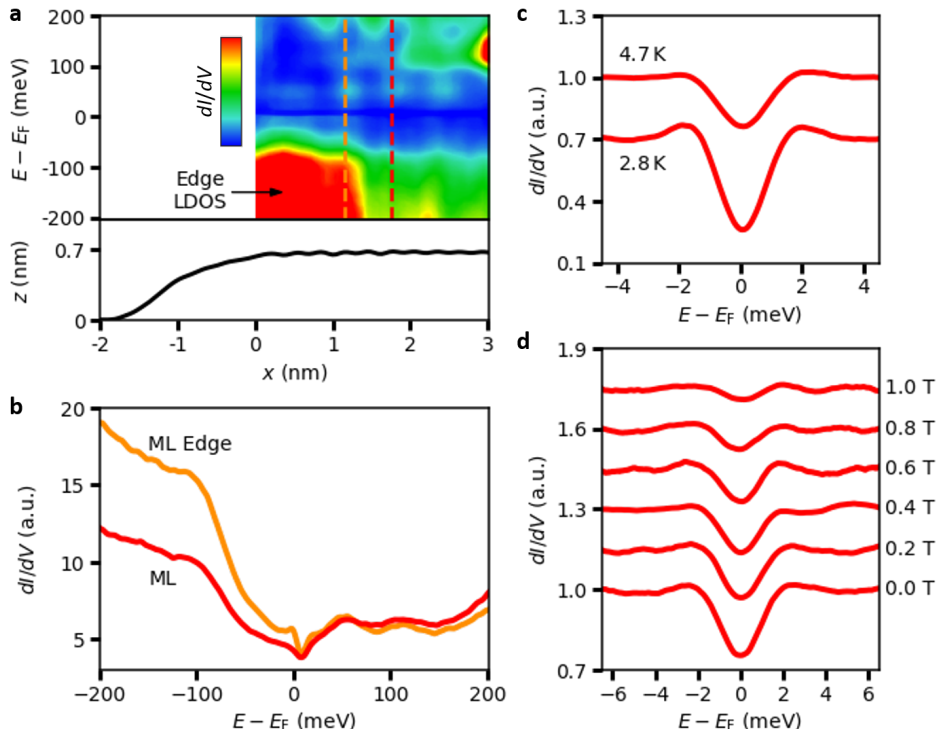


FIG. 2. **Simultaneous presence of quantum spin Hall edge state and superconducting gap on monolayer WTe₂.** (a) dI/dV spectra taken along a line across the step edge of the WTe₂ flake (top), and corresponding height profile (bottom) (b) Spatially averaged dI/dV spectra of monolayer WTe₂ showing a representative spectrum away from the monolayer edge (corresponding to the red dashed line in (a)) and increased density of states at the monolayer edge due to presence of the QSH edge state (corresponding to orange dashed line in (a)). Modulation amplitude $V_{\text{mod}} = 5$ mV. (c) Small voltage range dI/dV spectrum of monolayer WTe₂ at 4.7 K and 2.8 K showing superconducting gap-like features ($V_{\text{mod}} = 0.1$ mV). The 2.8 K curve is offset for clarity. (d) Magnetic field dependence of the small voltage range spectrum measured on the WTe₂ monolayer at 4.7 K. The curves are offset for clarity.

lations of the ML WTe₂/NbSe₂ heterostructure, which show only minimal modifications of the WTe₂ electronic structure compared to a freestanding WTe₂ ML (see Supplementary Materials).

Measurements of the ML WTe₂ dI/dV spectrum over a smaller voltage range (Fig. 2c), reveal a new feature: a superconducting gap-like feature characterized by a dip in the dI/dV signal at the Fermi energy, with peaks on either side of the gap. Comparison of measurements at 4.7 K and 2.8 K show that the gap deepens and the peaks sharpen at lower temperature. The evolution of the superconducting gap-like feature under application of a surface-normal magnetic field at 4.7 K (Fig. 2d) shows that with increasing magnetic field, the gap becomes less deep and the peaks flatten out until the gap features have nearly vanished at 1 T. We find that a fit of the Bardeen-Cooper-Schrieffer (BCS) model describes both the monolayer WTe₂ and the NbSe₂ data well (Fig. 3a). For NbSe₂, the fit results in a superconducting gap of $\Delta_{\text{NbSe}_2} = (0.84 \pm 0.01)$ meV, while for the WTe₂ we find $\Delta_{\text{WTe}_2}^{(\text{ML})} = (0.72 \pm 0.02)$ meV. In addition to following the trend of a superconducting gap with applied magnetic field, the vanishing of the gap near 1 T is similar to the Ginzburg-Landau estimate for the upper critical field of bulk

NbSe₂ [23]. We conclude that the gap feature observed on the ML WTe₂ is indeed a superconducting gap.

In order to confirm the proximity-induced nature of the observed superconducting gap on the WTe₂, we explore its evolution as a function of WTe₂ thickness. The exfoliation procedure naturally produces terraces of varying thickness in our samples, enabling thickness-dependent gap measurement within a single sample. Figure 3b shows the superconducting gap measured on terraces of different numbers of WTe₂ layers N , revealing that the gap decreases with increasing N , as expected for decaying superconducting correlations near the boundary of a superconducting-metal interface [24]. To quantify this behavior, we fit the BCS model to each of the spectra in Fig. 3b and plot the extracted gap sizes as filled circles in Fig. 3c. In the thick limit ($N \geq 3$), we find that observed behavior shows excellent agreement with transport measurements of proximity-induced superconductivity in bulk WTe₂ flakes [24, 25], extending the previous studies to the ultra-thin limit (see Supplementary Materials). For $N < 3$, we observe a more rapid decrease of the extracted gap as function of N which may be explained by the strong variation of the electronic structure of the WTe₂ in this thickness range, resulting in a larger mismatch of the

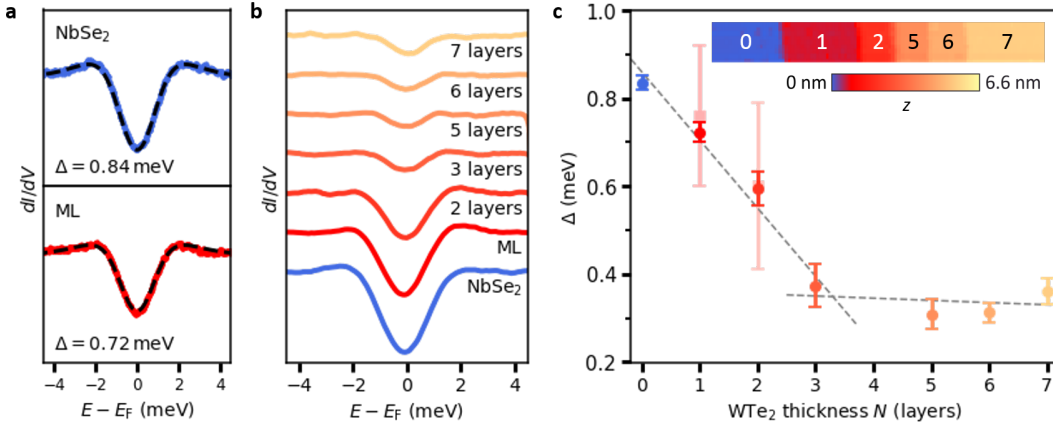


FIG. 3. **Evolution of the superconducting gap with WTe₂ thickness at 4.7 K.** (a) Fits of the BCS model to the superconducting gap spectra measured on NbSe₂ and monolayer WTe₂. (b) Measurement of the superconducting gap spectrum for WTe₂ layer thicknesses up to 7 layers. (c) (Filled circles) WTe₂ thickness dependence of the superconducting gap size obtained from fitting the spectra in (b) with the BCS gap equation. (Filled squares) Fits of the monolayer and bilayer spectrum with a more detailed model which includes partial tunneling into the NbSe₂ substrate. The dashed lines are guides to the eye and indicate two different regimes in which Δ decreases more rapidly for $N < 3$ and more gradually for $N \geq 3$. The inset shows a large-scale topography image of the WTe₂, where terraces of different WTe₂ thicknesses are observed. Scan size: 200 nm \times 14 nm. The corresponding number of WTe₂ layers N is indicated for each terrace, where $N = 0$ is the bare NbSe₂.

WTe₂ and NbSe₂ Fermi surfaces and therefore a stronger dependence of the induced gap on N [26]. For monolayer and bilayer WTe₂, we also consider the possibility of tunneling spectra being a superposition of tunneling into WTe₂ and into NbSe₂ (Fig. 4b inset). To isolate the respective contributions, we performed a control experiment on a second sample, in which we placed a ~ 20 nm thick layer of insulating hBN between the WTe₂ and NbSe₂ to locally decouple the WTe₂ (Fig. 4a, b). By comparing the measured dI/dV signal at the Fermi energy of spectra taken on WTe₂/hBN (A) and WTe₂/NbSe₂ (B), we find that the fractional contribution of tunneling into ML WTe₂ on the NbSe₂ is $f_{\text{WTe}_2} \equiv A/(A+B) = 0.14 \pm 0.04$. The NbSe₂ contribution is correspondingly $f_{\text{NbSe}_2} = B/(A+B) = 0.86 \pm 0.04$, i.e. the majority of the tunneling current. Knowing the relative WTe₂ contribution allows us to perform a more detailed analysis of the superconducting ML WTe₂/NbSe₂ spectrum (Fig. 4d) by fitting a superposition of WTe₂ and NbSe₂ BCS spectra with the same fractional contributions, i.e. $(dI/dV)_{\text{Total}} = f_{\text{WTe}_2} \cdot (dI/dV)_{\text{WTe}_2} + f_{\text{NbSe}_2} \cdot (dI/dV)_{\text{NbSe}_2}$, using a BCS form for each dI/dV (details in Supplementary Materials). The resulting proximity-induced gap sizes from the more detailed analysis are $\Delta_{\text{WTe}_2}^{(\text{ML})} = (0.76 \pm 0.16)$ meV at 4.7 K and (0.83 ± 0.08) meV at 2.8 K. For bilayer WTe₂ on NbSe₂, using a similar procedure, we find an induced gap of $\Delta_{\text{WTe}_2}^{(\text{BL})} = (0.60 \pm 0.19)$ meV. In Fig. 3c we also plot the 4.7 K WTe₂ proximity gaps found from this more detailed fitting and find no significant deviation from those previously determined by fitting the single-gap BCS theory. This observation is in qualitative agreement with theory which predicts the proximity-induced gap to approach that of the NbSe₂ as the WTe₂ layer thickness goes to zero [24].

Finally, we consider the lateral variation of the superconducting gap from within the ML WTe₂ to the region occupied by the edge state. Figure 4c shows dI/dV spectra taken at 2.8 K along a line approaching the physical edge of the WTe₂ monolayer, similar to that shown in Fig. 2a but over a smaller voltage range. We find that the superconducting gap is present throughout the WTe₂ monolayer with only slight changes in the gap width and depth. It is apparent that a superconducting gap is present in the region in which the QSH edge state is observed in Fig. 2a (indicated by the dashed line in Fig. 4c). To determine the fractional contribution of the WTe₂ edge spectrum, in Fig. 4e we perform a similar fit as we did for the spectrum away from the edge (Fig. 4d), using the same absolute NbSe₂ background as in Fig. 4d, but the larger conductance for of the WTe₂, corresponding to the larger tunneling conductance into the edge state at the Fermi energy (Fig. 2b). The resulting relative contribution of the edge state is $f_{\text{WTe}_2} = 0.33 \pm 0.06$ and the extracted gap size is $\Delta_{\text{WTe}_2}^{(\text{edge})} = (0.75 \pm 0.08)$ meV.

The observation of a superconducting gap in the edge state of monolayer 1T'-WTe₂ provides strong evidence that we have created a 1D topological superconductor in a van der Waals heterostructure by proximity-induced superconductivity in the quantum spin Hall edge state. The topological nature of a superconducting QSH edge state could be explicitly demonstrated in an STM measurement by creating a boundary with a portion of the same QSH edge state in which a topologically-trivial gap has been opened [4]. This would localize Majorana zero modes at the boundary, which can be identified as a zero-bias conductance peak within the superconducting gap [27]. Creating such a boundary is straightforward in the van der Waals material platform, e.g., by integrat-

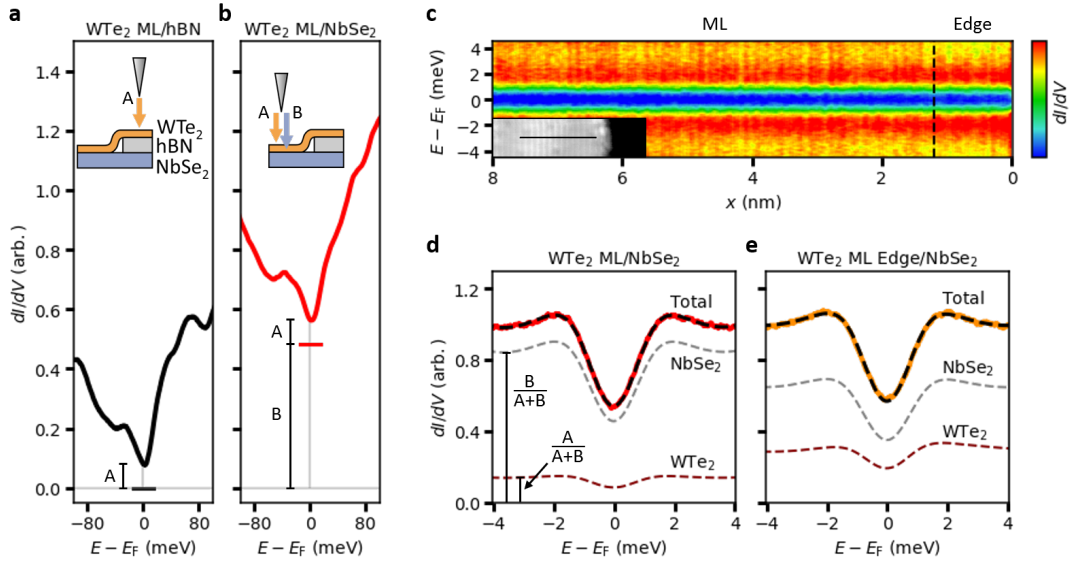


FIG. 4. **Proximity-induced superconducting gap in the quantum spin Hall edge state of monolayer WTe₂ at 2.8 K.** (a) Tunneling spectrum of WTe₂ on hexagonal boron nitride (hBN) and (b) spectrum of the *same* WTe₂ flake on NbSe₂ (for optical micrograph of the heterostructure see Supplementary Materials). The tunneling contributions of the WTe₂ and NbSe₂ are denoted as *A* and *B*, respectively. (c) SC gap spectra measured along a line perpendicular to the edge of the WTe₂. The inset shows the topography and line along which the spectra were taken. Scan size: 16 nm × 4 nm. (d) Fitting of representative ML WTe₂/NbSe₂ tunneling spectrum with fractional WTe₂ and NbSe₂ contributions determined from (a) and (b). The grey and maroon dashed lines indicate the relative contributions $(dI/dV)_{\text{NbSe}_2}$ and $(dI/dV)_{\text{WTe}_2}$. (e) Fitting of the ML edge WTe₂/NbSe₂ tunneling spectrum with fractional WTe₂ and NbSe₂ contributions determined as for (d) but with the increased DOS of the edge state.

ing a van der Waals magnetic insulator into the heterostructure shown in Fig. 1a to open a local Zeeman gap. Our work establishes the groundwork for such an experiment with a clear path toward the realization of Majorana quasiparticles. In addition, the method of sample preparation outlined in this work may be easily adapted to numerous experiments involving surface-probe studies or air-sensitive materials.

Acknowledgments. The authors acknowledge Di Xiao, David Cobden and Xiaodong Xu for helpful discussions and Nicholas Speeney and Nicolas Iskos for assistance in the lab. B.M.H. was supported by the Department of Energy under the Early Career award program (DE-SC0018115). Crystal growth and characterization at ORNL was supported by the US Department of Energy, Office of Science, Basic Energy Sciences, Division of Materials Sciences and Engineering. The authors thank the Pennsylvania State University Two-Dimensional Crystal Consortium - Materials Innovation Platform (2DCC-MIP) which is supported by NSF DMR-1539916 for supplying further 2D materials. F.L. and D.W. were supported by the NSF DMR-1809145 for the STM measurements. The authors gratefully acknowledge NSF DMR-1626099 for acquisition of the STM instrument. S.C.d.l.B. was supported by the Department of Energy (DE-SC0018115) for fabrication of proximity-effect van der Waals heterostructures. DFT Calculations were supported by the Department of Energy under grant DE-SC0014506.

Author contributions. F.L., D.W., R.M.F. and B.M.H. designed the experiment. F.L. and D.W. acquired the experimental data and F.L., D.W., and R.M.F. analyzed the data. F.L., D.W. and S.C.d.l.B. fabricated the samples. F.L., D.W., S.C.d.l.B., R.M.F. and B.M.H. wrote the manuscript, and all authors commented on the manuscript. J.Y. grew the WTe₂ crystals. D.M. provided other van der Waals crystals used in this study. M.W. performed DFT calculations. R.M.F. and B.M.H. supervised the project.

-
- [1] S. Tang, C. Zhang, D. Wong, Z. Pedramrazi, H.-Z. Tsai, C. Jia, B. Moritz, M. Claassen, H. Ryu, S. Kahn, J. Jiang, H. Yan, M. Hashimoto, D. Lu, R. G. Moore, C.-C. Hwang, C. Hwang, Z. Hussain, Y. Chen, M. M. Ugeda, Z. Liu, X. Xie, T. P. Devereaux, M. F. Crommie, S.-K. Mo, Z.-X. Shen, Quantum spin Hall state in monolayer 1T'-WTe₂. *Nat. Phys.* **13**, 683 (2017).
 - [2] Z. Fei, T. Palomaki, S. Wu, W. Zhao, X. Cai, B. Sun, P. Nguyen, J. Finney, X. Xu, D. H. Cobden, Edge conduction in monolayer WTe₂. *Nat. Phys.* **13**, 677 (2017).
 - [3] S. Wu, V. Fatemi, Q. D. Gibson, K. Watanabe, T. Taniguchi, R. J. Cava, P. Jarillo-Herrero, Observation of the quantum spin Hall effect up to 100 Kelvin in a monolayer crystal. *Science* **359**, 76 (2018).
 - [4] J. Alicea, New directions in the pursuit of Majorana fermions in solid state systems. *Rep. Prog. Phys.* **75**, 076501 (2012).
 - [5] A. Y. Kitaev, Unpaired Majorana fermions in quantum wires. *Phys.-Uspekhi* **44**, 131 (2001).

- [6] L. Fu, C. L. Kane, Superconducting proximity effect and Majorana fermions at the surface of a topological insulator. *Phys. Rev. Lett.* **100**, 096407 (2008).
- [7] S. Das Sarma, M. Freedman, C. Nayak, Majorana zero modes and topological quantum computation. *npj Quantum Inf.* **1**, 15001 (2015).
- [8] M. Sato, Y. Ando, Majorana zero modes and topological quantum computation. *Rep. Prog. Phys.* **80**, 076501 (2017).
- [9] Y. Maeno, S. Kittaka, T. Nomura, S. Yonezawa, K. Ishida, Evaluation of spin-triplet superconductivity in Sr_2RuO_4 . *J. Phys. Soc. Jpn.* **81**, 011009 (2012).
- [10] L. Fu, C. L. Kane, Josephson current and noise at a superconductor/quantum-spin-Hall-insulator/superconductor junction. *Phys. Rev. B* **79**, 161408 (2009).
- [11] M.-X. Wang, C. Liu, J.-P. Xu, F. Yang, L. Miao, M.-Y. Yao, C. L. Gao, C. Shen, X. Ma, X. Chen, Z.-A. Xu, Y. Liu, S.-C. Zhang, D. Qian, J.-F. Jia, Q.-K. Xue, The coexistence of superconductivity and topological order in the Bi_2Se_3 thin films. *Science* **336**, 52 (2012).
- [12] H.-H. Sun, K.-W. Zhang, L.-H. Hu, C. Li, G.-Y. Wang, H.-Y. Ma, Z.-A. Xu, C.-L. Gao, D.-D. Guan, Y.-Y. Li, C. Liu, D. Qian, Y. Zhou, L. Fu, S.-C. Li, F.-C. Zhang, J.-F. Jia, Majorana zero mode detected with spin selective Andreev reflection in the vortex of a topological superconductor. *Phys. Rev. Lett.* **116**, 257003 (2016).
- [13] S. Hart, H. Ren, T. Wagner, P. Leubner, M. Mühlbauer, C. Brüne, H. Buhmann, L. W. Molenkamp, A. Yacoby, Induced superconductivity in the quantum spin Hall edge. *Nat. Phys.* **10**, 638 (2014).
- [14] E. Bocquillon, R. S. Deacon, J. Wiedenmann, P. Leubner, T. M. Klapwijk, C. Brüne, K. Ishibashi, H. Buhmann, L. W. Molenkamp, Gapless Andreev bound states in the quantum spin Hall insulator HgTe . *Nat. Nanotechnol.* **12**, 137 (2016).
- [15] X. Qian, J. Liu, L. Fu, J. Li, Quantum spin Hall effect in two-dimensional transition metal dichalcogenides. *Science* **346**, 1344 (2014).
- [16] Z.-Y. Jia, Y.-H. Song, X.-B. Li, K. Ran, P. Lu, H.-J. Zheng, X.-Y. Zhu, Z.-Q. Shi, J. Sun, J. Wen, D. Xing, S.-C. Li, Direct visualization of a two-dimensional topological insulator in the single-layer $1\text{T}'\text{-WTe}_2$. *Phys. Rev. B* **96**, 041108 (2017).
- [17] L. Peng, Y. Yuan, G. Li, X. Yang, J.-J. Xian, C.-J. Yi, Y.-G. Shi, Y.-S. Fu, Observation of topological states residing at step edges of WTe_2 . *Nat. Commun.* **8**, 659 (2017).
- [18] Y. Shi, J. Kahn, B. Niu, Z. Fei, B. Sun, X. Cai, B. A. Francisco, D. Wu, Z.-X. Shen, X. Xu, D. H. Cobden, Y.-T. Cui, Imaging quantum spin Hall edges in monolayer WTe_2 . *Sci. Adv.* **5** (2019).
- [19] V. Fatemi, S. Wu, Y. Cao, L. Brethau, Q. D. Gibson, K. Watanabe, T. Taniguchi, R. J. Cava, P. Jarillo-Herrero, Electrically tunable low-density superconductivity in a monolayer topological insulator. *Science* **362**, 926 (2018).
- [20] E. Sajadi, T. Palomaki, Z. Fei, W. Zhao, P. Bement, C. Olsen, S. Luescher, X. Xu, J. A. Folk, D. H. Cobden, Gate-induced superconductivity in a monolayer topological insulator. *Science* **362**, 922 (2018).
- [21] Y. Zeng, J. I. A. Li, S. A. Dietrich, O. M. Ghosh, K. Watanabe, T. Taniguchi, J. Hone, C. R. Dean, High-quality magnetotransport in graphene using the edge-free Corbino geometry. *Phys. Rev. Lett.* **122**, 137701 (2019).
- [22] I. Cucchi, I. Gutierrez-Lezama, E. Cappelli, S. McKeown Walker, F. Y. Bruno, G. Terasini, L. Wang, N. Ubrig, C. Barretero, E. Giannini, M. Gibertini, A. Tamai, A. F. Morpurgo, F. Baumberge, Microfocus laser angle-resolved photoemission on encapsulated mono-, bi-, and few-layer $1\text{T}'\text{-WTe}_2$. *Nano Lett.* **19**, 554 (2019).
- [23] P. Garoche, J. J. Veyssi, P. Manuel, P. Molini, Experimental investigation of superconductivity in 2H-NbSe_2 single crystal. *Solid State Commun.* **19**, 455 (1976).
- [24] C. Huang, A. Narayan, E. Zhang, Y. Liu, X. Yan, J. Wang, C. Zhang, W. Wang, T. Zhou, C. Yi, S. Liu, J. Ling, H. Zhang, R. Liu, R. Sankar, F. Chou, Y. Wang, Y. Shi, K. T. Law, S. Sanvito, P. Zhou, Z. Han, F. Xiu, Inducing strong superconductivity in WTe_2 by a proximity effect. *ACS Nano* **12**, 7185 (2018).
- [25] Q. Li, C. He, Y. Wang, E. Liu, M. Wang, Y. Wang, J. Zeng, Z. Ma, T. Cao, C. Yi, N. Wang, K. Watanabe, T. Taniguchi, L. Shao, Y. Shi, X. Chen, S.-J. Liang, Q.-H. Wang, F. Miao, Proximity-induced superconductivity with subgap anomaly in type II Weyl semi-metal WTe_2 . *Nano Lett.* **18**, 7962 (2018).
- [26] C. R. Reeg, D. L. Maslov, Hard gap in a normal layer coupled to a superconductor. *Phys. Rev. B* **94**, 020501 (2016).
- [27] B. Jäck, Y. Xie, J. Li, S. Jeon, B. A. Bernevig, A. Yazdani, Observation of a Majorana zero mode in a topologically protected edge channel. *Science* **364**, 1255 (2019).

Supplementary Materials:

Proximity-induced superconducting gap in the quantum spin Hall edge state of monolayer WTe_2

Felix Lüpke,^{1*} Dacen Waters,^{1*} Sergio C. de la Barrera,¹ Michael Widom,¹
David G. Mandrus,^{2,3,4} Jiaqiang Yan,² Randall M. Feenstra,¹ and Benjamin M. Hunt^{1†}

¹*Department of Physics, Carnegie Mellon University, Pittsburgh, PA 15213, USA*

²*Materials Science and Technology Division, Oak Ridge National Laboratory, Oak Ridge, TN 37831, USA*

³*Department of Materials Science and Engineering, University of Tennessee, Knoxville, TN 37996, USA*

⁴*Department of Physics and Astronomy, University of Tennessee, Knoxville, TN 37996, USA*

* These authors contributed equally

†E-mail: bmhunt@andrew.cmu.edu

SAMPLE FABRICATION

The newly developed sample fabrication method consists of the following steps:

1. Mechanically exfoliate NbSe_2 and WTe_2 onto O_2 -plasma-cleaned SiO_2/Si wafer in a nitrogen-filled glove box (Fig. S1a and b).
2. Using a PPC/PDMS droplet transfer slide [S1], pick up the NbSe_2 flake, then pick up the WTe_2 flake. The transfer stage temperature is $\approx 40^\circ\text{C}$ for both pick ups.
3. Peel off the PPC layer from the PDMS, flip it upside down and put it onto a second transfer slide which has a PDMS droplet on it into which a hole was cut such that the heterostructure sits in the center of the hole and does not touch the PDMS.
4. Place the heterostructure onto pre-evaporated gold leads (Au (50 nm)/Pd (30 nm)/Cr (10 nm)) on an SiO_2/Si chip which is mounted on an STM sample plate and wire bonded to contacts sitting on the sample plate. Release the PPC by heating it to 100°C .
5. With the sample still at 100°C , remove some of the PPC surrounding the heterostructure using a sharp needle (Fig. S1c). This step prevents the heterostructure from floating off of the gold lead in the next step.
6. Transfer the sample from the glovebox into vacuum (without exposing it to air), and anneal it at 250°C for 8 h ($p \leq 1 \cdot 10^{-5}$ mBar) to remove the PPC. We perform this step using a tube furnace which has a gate valve attached to it and is vented with nitrogen. Subsequently, transfer the sample to the STM ultra-high vacuum chamber and perform a final annealing step at 250°C for ~ 10 mins ($p \leq 1 \cdot 10^{-8}$ mBar) before introducing the sample into the STM.

Using this technique, in contrast to previously reported dry-transfer techniques, the final top surface of the assembled van der Waals heterostructure is never in contact with any polymer or solvent. We find this to be crucial to achieve atomically-clean surfaces. Furthermore, sample fabrication is performed entirely in an inert gas/vacuum environment. This allows to study the pristine surfaces of highly air-sensitive materials, the only constraint being that the materials do not degrade when annealed at 250°C in vacuum.

For the samples presented in the main text, WTe_2 flakes were transferred onto ~ 20 nm thick NbSe_2 flakes. At this thickness, the electronic properties of the NbSe_2 are bulk-like and the critical temperature below which the NbSe_2 becomes superconducting is $T_c \approx 7$ K [S2]. Figure S1 shows optical images of the sample studied in the main text, except in Fig. 4a and b.

SCANNING TUNNELING MEASUREMENTS

The STM tip is approached to the $\text{WTe}_2/\text{NbSe}_2$ heterostructure using a capacitive technique adapted from Ref. S3. The commercial CreaTec STM helium bath temperature is 4.2 K with the ability of intermittently reaching ~ 1 K by pumping on the cryostat. The resulting temperatures of the STM base plate are 4.7 K and 2.8 K, respectively, due to vibration isolation and optical access. The STM is equipped with an electrochemically-etched tungsten tip which was cleaned by indentation into gold prior to and in between measurements. The lock-in frequency was set to $f = 925$ Hz in all dI/dV measurements. All

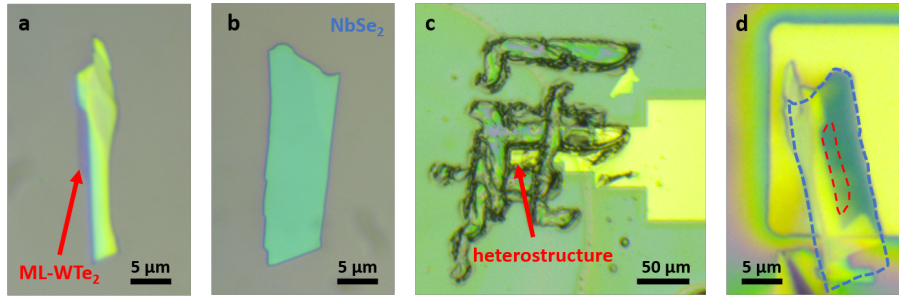


FIG. S1. **Fabrication of the $WTe_2/NbSe_2$ heterostructure.** (a), (b) Optical image of the WTe_2 and $NbSe_2$ flake after exfoliation onto SiO_2 . (c) Optical image after putting down the flipped heterostructure onto the gold lead and removing some of the PPC surrounding the flake using a sharp needle. (d) Optical image showing the heterostructure on the gold lead after vacuum annealing. Red and blue dashed lines indicate the outlines of the WTe_2 monolayer and $NbSe_2$, respectively.

superconducting gap measurements were performed at $V_{\text{sample}} = 5$ mV with $V_{\text{mod}} = 100$ μ V peak-to-peak and $I_t = 100$ pA, except in Fig. 2e where $V_{\text{sample}} = 10$ mV. The spectra in Fig. 2a and b were acquired using $V_{\text{sample}} = 300$ mV, $I_t = 400$ pA and $V_{\text{mod}} = 5$ mV. In Fig. 4, tunneling parameters are: $V_{\text{sample}} = 300$ mV, $I_t = 100$ pA and $V_{\text{mod}} = 5$ mV in (a) and $V_{\text{sample}} = 300$ mV, $I_t = 110$ pA and $V_{\text{mod}} = 10$ mV in (b). For quantitative comparison, the spectra in Fig. 4a and b and Fig. S3c were normalized to I_t and V_{mod} , respectively.

MOIRÉ EFFECTS

Figure S2a shows an STM image where both the moiré periodicity and the atomic rows of the ML $WTe_2/NbSe_2$ heterostructure can be seen. Analyzing atomic resolution images of the WTe_2 and $NbSe_2$ close to the WTe_2 step edge, we find a small rotational misalignment of $\sim 3^\circ$ between the WTe_2 a -axis and the $NbSe_2$ (Fig. S2b and c). The resulting moiré period can be approximated as

$$L = \frac{a}{\sqrt{\Theta^2 + \varepsilon^2}} \quad (\text{S1})$$

where $a = 3.48$ \AA is the shorter WTe_2 lattice constant, ε is its relative lattice mismatch with respect to the $NbSe_2$ lattice constant ($\sim 1.1\%$) and $\Theta \approx 3^\circ$ is the rotational angle between the two materials [S4]. The resulting moiré period is $L \approx 6.5$ nm which is in good agreement with the periodicity observed in the STM image. Note that the moiré period in direction of the WTe_2 b vector is negligibly small because the rotational misalignment of it with respect to the second $NbSe_2$ lattice vector is large.

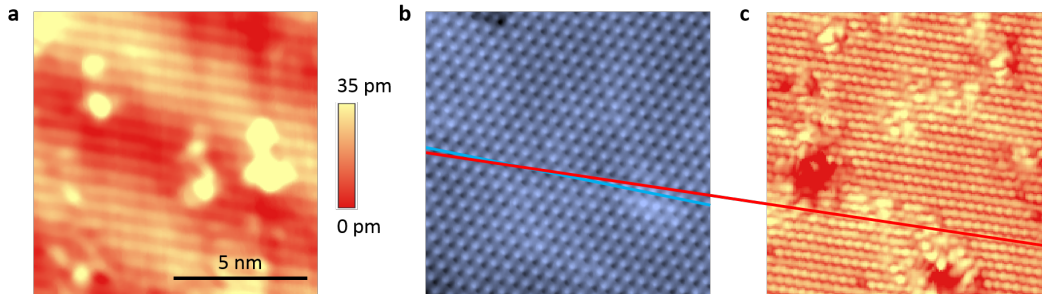


FIG. S2. **Observed moiré pattern.** (a) Topography image of the ML $WTe_2/NbSe_2$ heterostructure, showing the moiré periodicity and WTe_2 atomic rows ($V_{\text{sample}} = 1$ V and $I_t = 50$ pA). (b) Atomic resolution image of $NbSe_2$ right below the step edge of the WTe_2 . The blue line indicates the orientation of the $NbSe_2$ lattice vector. (c) Atomic resolution image of WTe_2 right next to the step edge. The red line indicates the orientation of the WTe_2 a -lattice vector. This misorientation with respect to the $NbSe_2$ is $\sim 3^\circ$.

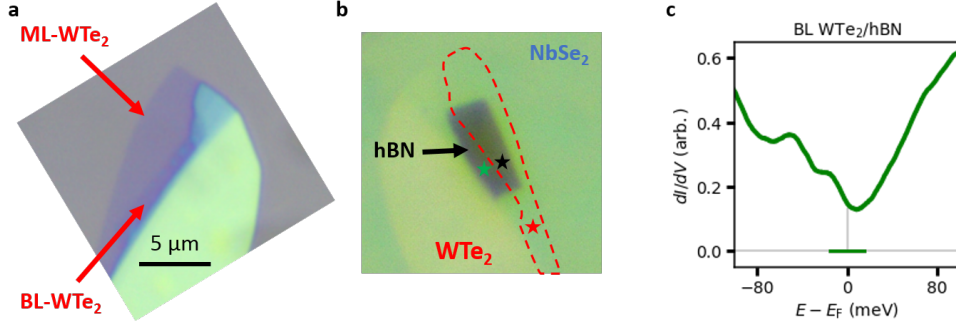


FIG. S3. **WTe₂/hBN/NbSe₂ heterostructure.** (a) Optical image of the WTe₂ flake after exfoliation, with indicated WTe₂ monolayer and bilayer regions. (b) Optical image of the assembled WTe₂/hBN/NbSe₂ heterostructure. The hBN thickness is ~ 20 nm and the NbSe₂ thickness is ~ 100 nm. The red, black and green stars indicate the positions at which spectra of ML WTe₂/hBN (Fig. 4a), ML WTe₂/NbSe₂ (Fig. 4b) and BL WTe₂/hBN (c) were taken, respectively.

BAND GAP IN ML WTe₂

While ARPES [S5] and transport measurements [S6] show indications of a band gap in the electronic structure of ML WTe₂, so far no hard gap has been observed in STM. Among the proposed explanations for a finite dI/dV signal at the Fermi energy are defect states and substrate effects [S5], a charge density wave [S7] and a Coulomb gap [S8], which we discuss below. By comparing the different STM studies of ML WTe₂ [S5, S7, S8], defect states seem to be an unlikely explanation because the non-zero dI/dV signal is observed even far away from topographic defects and the reported defect concentrations vary from study to study. While a CDW may explain the observed gap feature, the doping dependence of the band gap feature reported in Ref. S8 does not line up with a typical CDW behavior. Furthermore, the topographic CDW features are not well reproduced in reports other than in Ref. S7. Lastly, a Coulomb gap due to lateral hopping in ML WTe₂ was proposed as a possible explanation [S8]. This explanation is based on ML WTe₂ being decoupled from the substrate, which seems reasonable due to the van der Waals stacking and small Fermi surface overlap of ML WTe₂ and graphene as well as NbSe₂. To understand the origin of a possible Coulomb gap in more detail, we consider tip-induced band bending (TIBB) to play a crucial role. TIBB can have a significant effect on the measured dI/dV spectra and is known to lead to a finite dI/dV signal in the band gap [S9]. The 2D analog of 3D TIBB is a local band shift in the 2D layer. As a result, there is no additional confinement of states in the z -direction but only in the x - y plane, i.e. a laterally extended circular potential well. The depth of the potential well increases with decreasing tip-sample distance and decreasing STM tip work function and results in a local accumulation of charges at the position of the STM tip, i.e. a downward band shift. In the context of TIBB, the observed dip in the finite dI/dV signal at the Fermi energy can be explained as a Coulomb gap associated with the accumulation layer that is formed in the potential well. TIBB may also explain why the in-gap dI/dV signal and the signature of the Coulomb gap is weak in Ref. S5: in their experiments the current setpoint was lower (and the work function of their tip may have been higher), producing less TIBB and therefore fewer electrons in the accumulation layer compared to our results and Refs. S7, S8. Furthermore, the presence of a tip-induced electron accumulation layer in the WTe₂ can explain the reported conduction and valence band overlap extracted from quasi-particle interference (QPI) measurements in Ref. S8 which is in contrast to ARPES results [S5]: with the finite dI/dV signal in the band gap originating from the tip-induced electron accumulation layer, it is expected that the QPI of these states will yield wave vectors corresponding to the down-shifted conduction band states. As a result, QPI is expected to show conduction band wave vectors down to voltages beyond the actual conduction band edge and persist until they are dominated by the valence band conductance. In summary, we believe that TIBB may explain the majority of gap features reported in the literature.

SPECTRA FITTING

The finite-temperature differential conductance function that we fit to the spectroscopic data is the density of states convolved with the derivative of the Fermi function, i.e.

$$\frac{dI}{dV} \propto \int_{-\infty}^{\infty} dE \frac{\exp\left(\frac{E-eV}{k_B T_{\text{tip}}}\right)}{\left[\exp\left(\frac{E-eV}{k_B T_{\text{tip}}}\right) + 1\right]^2} N(E) \quad (\text{S2})$$

where $N(E)$ is the density of states of the sample and the density of states in the tip is assumed to be uniform. In standard BCS theory, the density of states N is given by

$$N(E, \Delta) = N_0 \text{Re} \left[\frac{E}{\sqrt{E^2 - \Delta^2}} \right] \quad (\text{S3})$$

where Δ is the gap size of the superconductor and N_0 is the normal state density of states, which is typically assumed to be constant. However, in experiments the differential conductance signal often shows a non-constant normal state conductance around the Fermi energy. To achieve representative fits of the superconducting gaps, we therefore allow for a normal state conductance background given by a low-order polynomial function which we fit simultaneously with the BCS gap function (this is then divided out of the superconducting gap spectra presented in the main text Figs. 2, 3, and 4). We fit the NbSe₂ spectra using a two-gap model [S2], which we find provides good fits at all temperatures. The density of states for the two-gap model is given by

$$N_{\text{NbSe}_2}(E, \Delta_1, \Delta_2) = CN(E, \Delta_1) + (1 - C)N(E, \Delta_2) \quad (\text{S4})$$

First, we fit data of Ref. S10 acquired at 100 mK, yielding gaps of $\Delta_{\text{NbSe}_2,1} = (1.1844 \pm 0.0021)$ meV and $\Delta_{\text{NbSe}_2,2} = 0.8300 \pm 0.0027$ meV (and a tip temperature of $T_{\text{tip}} = 1.0445 \pm 0.0134$ K). The amplitudes of the large-gap and small-gap terms are expressed by parameters C and $(1 - C)$, with a value of $C = 0.5424 \pm 0.0047$ found from this fit. This same value of C is then used in fits to our own NbSe₂ spectra, shown in Fig. S4. The resulting gap sizes are $\Delta_{\text{NbSe}_2,1} = 1.154 \pm 0.031$ meV and $\Delta_{\text{NbSe}_2,2} = 0.757 \pm 0.011$ meV with tip temperature of $T_{\text{tip}} = 5.962 \pm 0.033$ K at a base plate temperature of 2.8 K, and gaps of $\Delta_{\text{NbSe}_2,1} = 1.051 \pm 0.030$ and $\Delta_{\text{NbSe}_2,2} = 0.495 \pm 0.060$ meV with tip temperature of $T_{\text{tip}} = 7.405 \pm 0.052$ at a base plate temperature of 4.7 K. We find that the temperature dependence of the larger of these NbSe₂ gap values matches very well to the universal temperature behavior of a BCS superconducting gap. The temperature dependence of the smaller gap, however, does not agree as well with the universal BCS prediction. The sample temperatures in our experiments, extracted from the known temperature dependence of the NbSe₂ gaps, are approximately 1 K above our measured STM base plate temperatures.

Fitting of WTe₂ monolayer and monolayer edge on NbSe₂. Moving to the spectra acquired on the monolayer and the monolayer edge of WTe₂ on NbSe₂ and comparing those spectra to ones acquired on WTe₂ on hBN (Fig. 4 of the main text), we find that there is a significant contribution to the tunneling current from the underlying NbSe₂. We therefore fit our ML WTe₂ spectra with a three-gap model, two gaps of known size from the NbSe₂ and one induced gap from the WTe₂, $\Delta_{\text{WTe}_2}^{(\text{ML})}$, the size

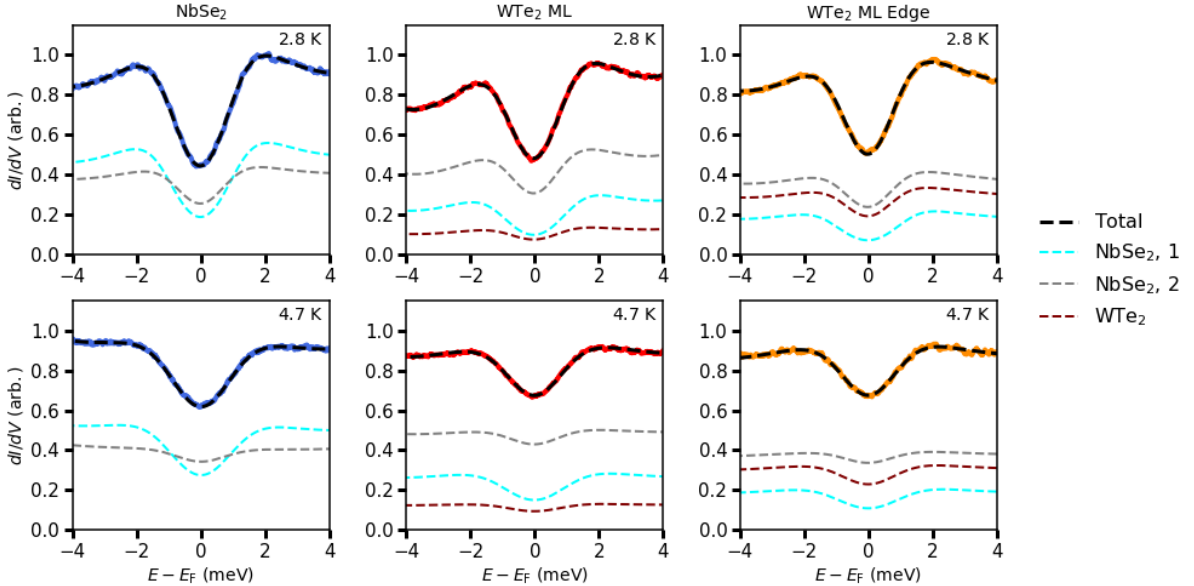


FIG. S4. **Fits of the superconducting gaps.** Representative raw data differential conductance spectra of NbSe₂ (left), WTe₂ ML away from the edge (center), and at the WTe₂ ML edge (right) at STM baseplate temperatures of 2.8 K (top) and 4.7 K (bottom). Best fits of Eq. S5 are shown as the thick black dashed lines. Thinner dashed lines indicate the relative contribution of each term in Eq. S5. All spectra taken at $V_{\text{sample}} = 5$ mV, $I_t = 100$ pA and $V_{\text{mod}} = 100$ μ V. In Fig. 4d and e of the main text, the two NbSe₂ contribution terms are combined for clarity.

	Parameter	2.8 K	4.7 K
NbSe ₂	$\Delta_{\text{NbSe}_2,1}$ (meV)	1.154 ± 0.031	1.051 ± 0.030
	$\Delta_{\text{NbSe}_2,2}$ (meV)	0.757 ± 0.011	0.495 ± 0.060
	C	0.5424 ± 0.0047 (fixed)	
	T_{tip} (K)	5.962 ± 0.033	7.405 ± 0.052
WTe ₂ monolayer	$\Delta_{\text{WTe}_2}^{(\text{ML})}$ (meV)	0.83 ± 0.08	0.76 ± 0.16
	f_{NbSe_2}	0.86 ± 0.04	
	C	0.33 ± 0.06	
WTe ₂ ML edge	$\Delta_{\text{WTe}_2}^{(\text{edge})}$ (meV)	0.75 ± 0.08	0.77 ± 0.08
	f_{NbSe_2}	0.65 ± 0.06	
	C	0.33 ± 0.06 (fixed)	
WTe ₂ bilayer	$\Delta_{\text{WTe}_2}^{(\text{BL})}$ (meV)	0.60 ± 0.19	
	f_{NbSe_2}	(min)0.25 – (max)1.00	
	C	(min)0.10 – (max)0.33	
WTe ₂ three layers	$\Delta_{\text{WTe}_2}^{(3\text{L})}$ (meV)	0.37 ± 0.05	
WTe ₂ five layers	$\Delta_{\text{WTe}_2}^{(5\text{L})}$ (meV)	0.31 ± 0.03	
WTe ₂ six layers	$\Delta_{\text{WTe}_2}^{(6\text{L})}$ (meV)	0.31 ± 0.02	
WTe ₂ seven layers	$\Delta_{\text{WTe}_2}^{(7\text{L})}$ (meV)	0.36 ± 0.03	

TABLE I. **Summary of fitting results.** Details described in the text.

of which is determined by fitting

$$N(E) = (1 - f_{\text{NbSe}_2})N(E, \Delta_{\text{WTe}_2}^{(\text{ML})}) + f_{\text{NbSe}_2}N_{\text{NbSe}_2}(E, \Delta_{\text{NbSe}_2,1}, \Delta_{\text{NbSe}_2,2}). \quad (\text{S5})$$

We fix the fractional contribution of the NbSe₂, $f_{\text{NbSe}_2} \equiv B/(A + B)$, by comparing the value of the observed conductance at the Fermi energy for ML WTe₂ on NbSe₂ and for ML WTe₂ on hBN. Importantly, for the NbSe₂ contribution, the relative amplitudes of the large-gap and small-gap terms is expected to differ from the $C = 0.5424 \pm 0.0047$ deduced above from bare NbSe₂, since the wave functions of the respective states will have varying decay constants as they extend through the WTe₂ and out into the vacuum. We therefore let C vary in the fits of the WTe₂ spectra. The tip temperatures are known from the fits to the bare NbSe₂ spectra and are fixed for fits of the spectra taken on the WTe₂.

To maximally constrain the fits, we simultaneously fit the spectra acquired at temperatures 2.8 K and 4.7 K, thus having three unknowns in total to fit the two spectra: the induced superconducting gap size for each, and the relative amplitude of the NbSe₂ large-gap and small-gap terms (i.e. the same value in both spectra). Using the best fit, midpoint values for all other ‘‘auxiliary’’ parameters (NbSe₂ gap sizes, sample temperatures, WTe₂ fractional contribution), we find values for the proximity-induced gaps in the WTe₂ of (0.80 ± 0.04) meV (at 2.8 K) and (0.73 ± 0.04) meV (at 4.7 K) and $C = 0.35 \pm 0.02$ (Fig. S4). To properly estimate error bounds for the induced gap, we further perform fits at the minimum and maximum values of the error range of all auxiliary parameters, thus yielding final values for the proximity-induced gaps for ML WTe₂ far from an edge of $\Delta_{\text{WTe}_2}^{(\text{ML})} = (0.83 \pm 0.08)$ meV and $\Delta_{\text{WTe}_2}^{(\text{ML})} = (0.76 \pm 0.16)$ meV, respectively at 2.8 K and 4.7 K, and $C = 0.33 \pm 0.04$. For the case of the WTe₂ ML edge on NbSe₂, we fit a spectrum acquired at 2.8 K using the known NbSe₂ gaps and known tip temperature, with f_{NbSe_2} determined to be 0.65 ± 0.06 by comparison of the edge spectrum (Fig. 2b) with those of the non-edge WTe₂ on NbSe₂ and WTe₂ on hBN (we make this indirect comparison because it is not possible to measure ML edge spectra on hBN, which would require there to be an exposed insulating hBN surface). We fit the edge spectrum using the value of $C = 0.33 \pm 0.04$, which we obtained from the monolayer fits. The resulting fit is shown in Fig. S4, with induced gap of $\Delta_{\text{WTe}_2}^{(\text{edge})} = (0.75 \pm 0.08)$ meV. For the case of acquisition temperature 4.7 K (not shown), the same procedure yields an induced gap of $\Delta_{\text{WTe}_2}^{(\text{edge})} = (0.77 \pm 0.08)$ meV. We note that we are not able to achieve good fits of our WTe₂ data if we assume a constant WTe₂ contribution, i.e. one that does not have a superconducting gap.

Fitting of multilayer WTe₂ on NbSe₂. We now consider thicker WTe₂ on NbSe₂, for which we have measured tunneling spectra at 4.7 K (Fig. 3). For $N = 3$ or more layers of WTe₂ we fit the observed spectra with a single-gap model (Eq. S3), obtaining proximity-induced gaps in good agreement with the thickness-trend found in prior measurements of $N > 10$ layers of WTe₂ on SiO₂ [S11] as shown in Fig. S5. We conclude that the tunneling contribution of NbSe₂ to the observed spectra is negligible for $N \geq 3$. For the case of bilayer WTe₂ on NbSe₂, as for monolayer WTe₂/NbSe₂, we must estimate the contribution of the NbSe₂ to the bilayer WTe₂/NbSe₂ spectrum. To do so, we have measured a spectrum of bilayer WTe₂ on hBN (Fig. S3c), from which we find the tunneling conductance at the Fermi energy to be $1.8\times$ larger than that for ML WTe₂ on hBN, thus implying a *lower bound* for the contribution of WTe₂ itself to the spectrum of bilayer WTe₂ on NbSe₂ of $1.8 \times 0.14 = 0.25$,

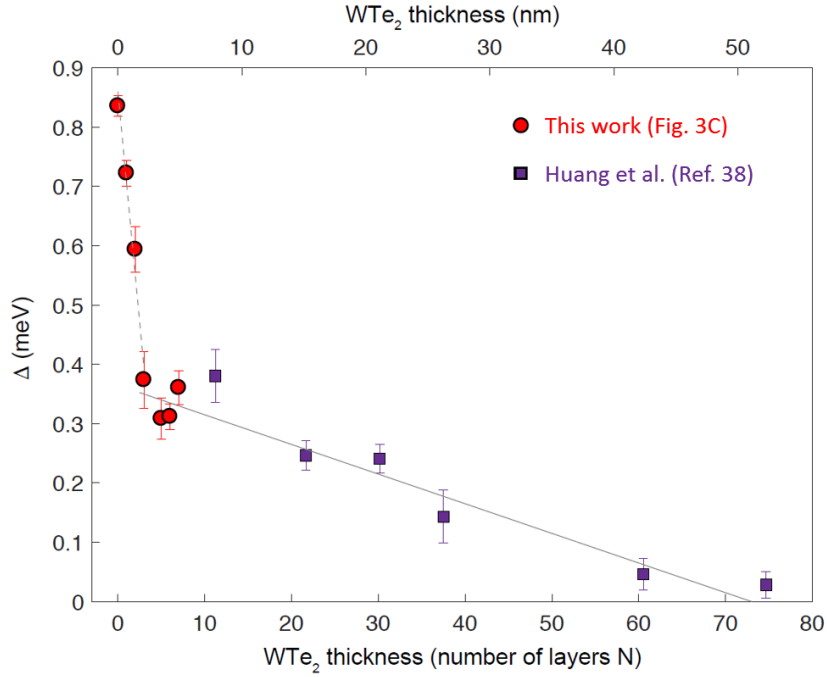


FIG. S5. **Comparison of observed superconducting gap thickness dependence to the literature.** Observed superconducting gap Δ vs. layer number N , from Fig. 3c of the main text (red circles) plotted alongside data extracted from transport measurements in Ref. S11 (purple squares). The grey dashed and grey solid lines, which are guides to the eye, show the trend of the observed gap size in the ‘thin’ limit ($N < 3$ layers) and ‘thick’ ($N \geq 3$ layers) limit respectively. The purple data points are calculated by extracting the $\Delta/\Delta_{\text{NbSe}_2}$ values from Fig. 5 in Ref. S11, taken at ≈ 2 K, and multiplying them by $\Delta_{\text{NbSe}_2} \approx 0.6$ meV at 4.7 K, a number obtained from Fig. 2g of the same paper ($\Delta_{\text{NbSe}_2} \equiv \Delta_0$ in that paper). This procedure is valid because the ratio $\Delta/\Delta_{\text{NbSe}_2}$ has a very weak temperature dependence (Fig. 2g of Ref. S11). This allows for direct comparison with our data, which were obtained at 4.7 K.

with the additional conservative assumption that the *total* tunneling current into the NbSe₂ on BL WTe₂/NbSe₂ is the same as on ML WTe₂/NbSe₂ (in general we expect the total tunneling into BL WTe₂/NbSe₂ to be less.) We therefore consider a range of WTe₂ fractional contributions for the bilayer case extending from 0.25 to 1.0. For the fractional magnitude of the NbSe₂ large-gap term, in the discussion above we found values of $C = 0.54$ and $C = 0.33$ for zero and one WTe₂ layer, respectively; thus, for two layers of WTe₂ we assume values in the range $C = 0.10 - 0.33$. Within these parameter ranges, we find a proximity-induced gap for the bilayer WTe₂ to be in the range $\Delta_{\text{WTe}_2}^{(\text{BL})} = 0.41 - 0.79$ meV, or $\Delta_{\text{WTe}_2}^{(\text{BL})} = (0.60 \pm 0.19)$ meV. Our fit results are summarized in Table I.

DENSITY FUNCTIONAL THEORY CALCULATIONS

We performed band structure calculations (Fig. S6) using density functional theory (DFT) in the generalized gradient approximation [S12] utilizing the projector augmented wave method as implemented in VASP [S13]. Lattice constants were set to orthorhombic WTe₂ values ($a = 3.477$ Å and $b = 6.249$ Å) for both the ML and the WTe₂/NbSe₂ bilayer, while we took $c = 30$ Å to allow sufficient vacuum. Atomic coordinates were relaxed holding the lattice constants fixed prior to calculating the band structure. The results for the freestanding WTe₂ monolayer, with and without spin-orbit-coupling (SOC) are shown in Fig. S6a and b. Note that in WTe₂ the bands near the Fermi energy originate mostly from the W atoms, the orbital character of which we plot as symbols as indicated in the figure legend. The calculations are in excellent agreement with previously reported band structures of 1T'-WTe₂. Especially, the inversion of bands with opposite parity is reproduced (marked as “+” and “-” in the figures). Note that the size of the gap, which opens when including SOC into the calculations is under predicted in DFT.

Next, we perform calculations which, in addition to the ML WTe₂, include a layer of NbSe₂ to model the present sample system. For this purpose, we construct a heterostructure unit cell which includes 2×1 unit cells of NbSe₂ and 1×1 unit cells of WTe₂. The NbSe₂ lattice parameter is adjusted such that the constructed unit cells match in size. We then let the structure relax, before calculating the supercell band structure, with and without SOC. Figures S6c and d show the resulting heterostructure bands, where we plot the W orbital character as symbols as before. The NbSe₂ bands near the Fermi energy are dominated by

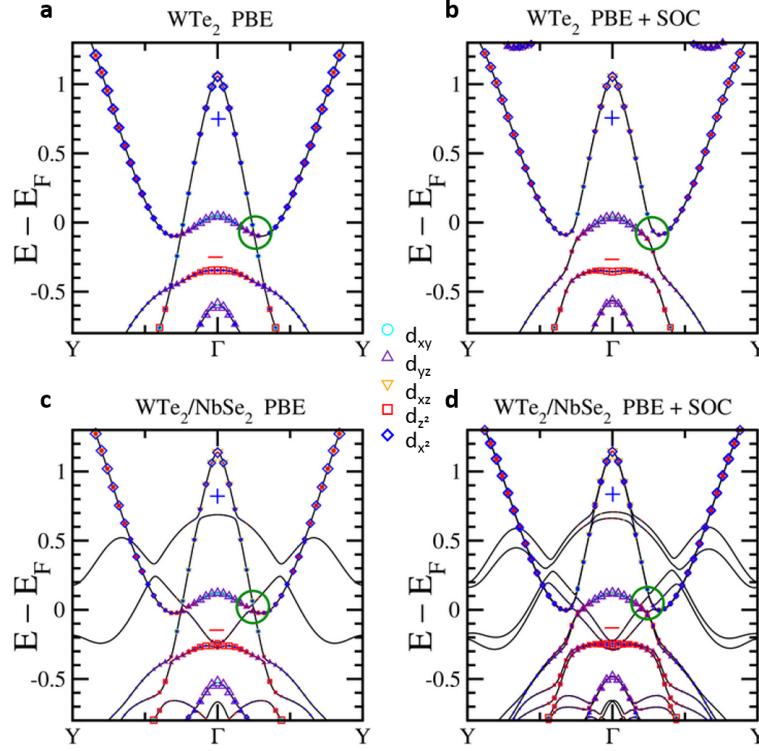


FIG. S6. **DFT band structure calculations.** (a) ML $1T'$ -WTe₂ without spin-orbit coupling (SOC) and (b) with SOC. (c) and (d) show the band structure for a heterostructure of ML $1T'$ -WTe₂ and a single layer of $2H$ -NbSe₂, respectively. Calculation details are described in the text. The green circle indicates where SOC forces bands to anti-cross in the pockets along the Y- Γ -Y path for both the ML WTe₂ and the heterostructure. The blue + and red - indicates the parity of the states associated with the band inversion resulting in the QSH edge state, in comparison to Fig. 2d and e from Ref. S5.

Nb which we plot without symbols. From the calculations, we find that the NbSe₂ has little effect on the the WTe₂ single-particle electronic structure, i.e. we observe no significant shifts of bands relative to each other and the band inversion is still present. There is only a small rigid upward shift of the WTe₂ bands (<100 meV) with respect to the calculated freestanding WTe₂ due to an NbSe₂ band near the Fermi level. Furthermore, we observe a slight hybridization between bands that originate in the NbSe₂ and the even parity conduction band of the WTe₂, but only at an energy well above the Fermi level. Note that the band splitting in Fig. S6d comes from the broken inversion symmetry due to the presence of the NbSe₂ which lifts the spin degeneracy of the bands when SOC is included. In conclusion, we find that the WTe₂ single-particle band structure, including the band inversion and therefore the QSH state, is preserved in the WTe₂/NbSe₂ heterostructure.

-
- [S1] L. Wang, I. Meric, P.Y. Huang, Q. Gao, Y. Gao, H. Tran, T. Taniguchi, K. Watanabe, L.M. Campos, D.A. Muller, J. Guo, P. Kim, J. Hone, K.L. Shepard, and C.R. Dean, One-Dimensional Electrical Contact to a Two-Dimensional Material. *Science* **342**, 614–617 (2013).
- [S2] E. Khestanova, J. Birkbeck, M. Zhu, Y. Cao, G.L. Yu, D. Ghazaryan, J. Yin, H. Berger, L. Forró, T. Taniguchi, K. Watanabe, R.V. Gorbachev, A. Mishchenko, A. K. Geim, and I. V. Grigorieva, Unusual suppression of the superconducting energy gap and critical temperature in atomically thin NbSe₂. *Nano Lett.* **18**, 2623–2629 (2018).
- [S3] G. Li, A. Luican, and E.Y. Andrei, Self-navigation of a scanning tunneling microscope tip toward a micron-sized graphene sample. *Rev. Sci. Instrum.* **82**, 073701 (2011).
- [S4] J. Jung, A. Raoux, Z. Qiao, A. H. MacDonald, Ab initio theory of moiré superlattice bands in layered two-dimensional materials. *Phys. Rev. B* **89**, 205414 (2014).
- [S5] S. Tang, C. Zhang, D. Wong, Z. Pedramrazi, H.-Z. Tsai, C. Jia, B. Moritz, M. Claassen, H. Ryu, S. Kahn, J. Jiang, H. Yan, M. Hashimoto, D. Lu, R. G. Moore, C.-C. Hwang, C. Hwang, Z. Hussain, Y. Chen, M. M. Ugeda, Z. Liu, X. Xie, T. P. Devereaux, M. F. Crommie, S.-K. Mo, Z.-X. Shen, Quantum spin Hall state in monolayer $1T'$ -WTe₂. *Nat. Phys.* **13**, 683 (2017).

- [S6] S. Wu, V. Fatemi, Q. D. Gibson, K. Watanabe, T. Taniguchi, R. J. Cava, P. Jarillo-Herrer, Observation of the quantum spin Hall effect up to 100 Kelvin in a monolayer crystal. *et al.*, *Science* **359**, 76 (2018).
- [S7] Z.-Y. Jia, Y.-H. Song, X.-B. Li, K. Ran, P. Lu, H.-J. Zheng, X.-Y. Zhu, Z.-Q. Shi, J. Sun, J. Wen, D. Xing, S.-C. Li, Direct visualization of a two-dimensional topological insulator in the single-layer 1T'-WTe₂. *Phys. Rev. B* **96**, 041108 (2017).
- [S8] Y.-H. Song, Z.-Y. Jia, D. Zhang, X.-Y. Zhu, Z.-Q. Shi, H. Wang, L. Zhu, Q.-Q. Yuan, H. Zhang, D.-Y. Xing, S.-C. Li, Observation of coulomb gap in the quantum spin Hall candidate single-layer 1T'-WTe₂. *Nat. Commun.* **9**, 4071 (2018).
- [S9] R. M. Feenstra, Tunneling spectroscopy of the (110) surface of direct-gap III-V semiconductors. *Phys. Rev. B* **50**, 4561 (1994).
- [S10] I. Guillamon, H. Suderow, F. Guinea, S. Vieira, Intrinsic atomic-scale modulations of the superconducting gap of 2H-NbSe₂. *Phys. Rev. B* **77**, 134505 (2008).
- [S11] C. Huang, A. Narayan, E. Zhang, Y. Liu, X. Yan, J. Wang, C. Zhang, W. Wang, T. Zhou, C. Yi, S. Liu, J. Ling, H. Zhang, R. Liu, R. Sankar, F. Chou, Y. Wang, Y. Shi, K. T. Law, S. Sanvito, P. Zhou, Z. Han, F. Xiu, Inducing strong superconductivity in WTe₂ by a proximity effect. *ACS Nano* **12**, 7185 (2018).
- [S12] J. P. Perdew, K. Burke, M. Ernzerhof, Generalized gradient approximation made simple. *Phys. Rev. Lett.* **77**, 3865 (1996).
- [S13] G. Kresse, D. Joubert, From ultrasoft pseudopotentials to the projector augmented-wave method. *Phys. Rev. B* **59**, 1758 (1999).